Geomechanics and Engineering, *Vol. 26, No. 6 (2021) 529-540*
https://doi.org/10.12989/gae.2021.26.6.529

Evaluating fiber-optic cable–soil mechanical coupling using elastoplastic pullout interaction modeling

Su-Ping Liu[1,2], Bin Shi[*1], Cheng-Cheng Zhang[**1,3], Kai Gu[1] and Pei-Zhi Zhuang[2,4]

[1]*School of Earth Sciences and Engineering, Nanjing University, Nanjing 210023, China*
[2]*School of Civil Engineering, University of Leeds, Leeds LS2 9JT, U.K.*
[3]*Nanjing University High-Tech Institute at Suzhou, Suzhou 215123, China*
[4]*School of Qilu Transportation, Shandong University, Jinan 250002, China*

(Received February 19, 2021, Revised August 23, 2021, Accepted September 14, 2021)

Abstract. The mechanical coupling between a fiber-optic cable and surrounding soil is a significant concern in distributed strain sensing-based geotechnical monitoring. In this study, the cable–soil mechanical coupling is quantitatively evaluated using elastoplastic pullout interaction modeling. Data from a laboratory pullout test performed on a 2-mm-diameter tight-buffered cable buried in a sand–gravel–clay mixture are used to validate a documented elastoplastic pullout model. By using cable axial strain profiles and cable–soil relative displacement measurements, two new indices are proposed to quantify the cable–soil mechanical coupling based on this model, in addition to the common interface shear strength proxy. A parametric study is conducted to investigate how the geometrical and mechanical properties of the cable and the cable–soil interface characteristics affect the two indices. Relating the parametric analysis to practical considerations, recommendations are made as to the design of strain-sensing cables for use in field and laboratory scenarios. Furthermore, modification to the elastoplastic pullout model is discussed to better simulate cable–soil pullout interactions. This study demonstrates that the elastoplastic pullout model can be effective in assessing cable–soil interface behavior and mechanical coupling.

Keywords: distributed strain sensing; elastoplastic model; geotechnical monitoring; interface behavior; pullout test

1. Introduction

Measurable soil deformation usually accompanies a host of geotechnical hazards such as slope failure, surface ruptures, sinkholes, and tunneling- and mining-induced settlement (Ashtiani *et al.* 2018, Mohamad *et al.* 2010, Ni *et al.* 2018, Szwedzicki 2001, Wang *et al.* 2020, Yang and Wang 2018, Liu *et al.* 2021a). Spatially continuous monitoring of soil deformation in situ is significantly useful for a better understanding of the mechanism of these hazards and the design and construction of appropriate mitigation measures accordingly. This can potentially be achieved by using the fiber-optic distributed strain sensing (DSS) technology—by integrating a fiber-optic cable into the geotechnical structure or soil, distributed strain profiles can be measured at high temporal resolution along the entire length of the cable up to tens of kilometers (Habel and Krebber 2011, Schenato 2017, Soga *et al.* 2019). In this context, DSS will complement traditional geotechnical instrumentation such as electrical resistance strain gauges, extensometers, and inclinometers for fine monitoring of the deformation of soil and geotechnical structures (Iten 2011, Friedli *et al.* 2019, Hauswirth *et al.* 2014, Moffat *et al.* 2015, Pelecanos *et al.* 2018, Puzrin *et al.* 2020, Schenato *et al.* 2017, Zhang *et al.* 2018a, b).

Compared with grouting or surface fixation to geotechnical structure, directly installing fiber-optic cables into soil means a difficult to quantify with precision the soil deformation using fiber-optic strain measurements, because primarily of the complex nature of the interaction between the embedded cable and the surrounding soil (Billon *et al.* 2015, Lanticq *et al.* 2009). In order to obtain accurate soil strain profiles, the mechanical properties and strain transfer behavior at the cable–soil interface have been a recent focus for geotechnical practitioners. For instance, Iten *et al.* (2009) used the Brillouin scattering-based DSS technique to obtain strain distributions along a soil-embedded fiber-optic cable at elevated pullout displacements and observed evident progressive failure behavior of the interface. Li *et al.* (2017) measured the deformation of a soil beam using both embedded fiber-optic cables and surface particle image velocimetry analysis; the cable–soil coupling performance was evaluated by comparing the two strain measurements. Winters *et al.* (2020) assessed the frictional resistance between a fiber-optic cable and variable confining soils (including gravel, sand, clay, and flowable fill) under controlled laboratory conditions. These reported tests have focused on testing the cable–soil interface characteristics while in-depth theoretical analysis is lacking.

With regards to analytical modeling, the soil-to-cable strain transfer is achieved by shearing between the cable and the soil (Zhang *et al.* 2020). As such, the soil-embedded fiber-optic cable behaves likely as a continuously frictionally coupled (CFC) system, where the interface

*Corresponding author, Professor
E-mail: shibin@nju.edu.cn
**Corresponding author, Assistant Professor
E-mail: zhang@nju.edu.cn

ISSN: 2005-307X (Print), 2092-6219 (Online)

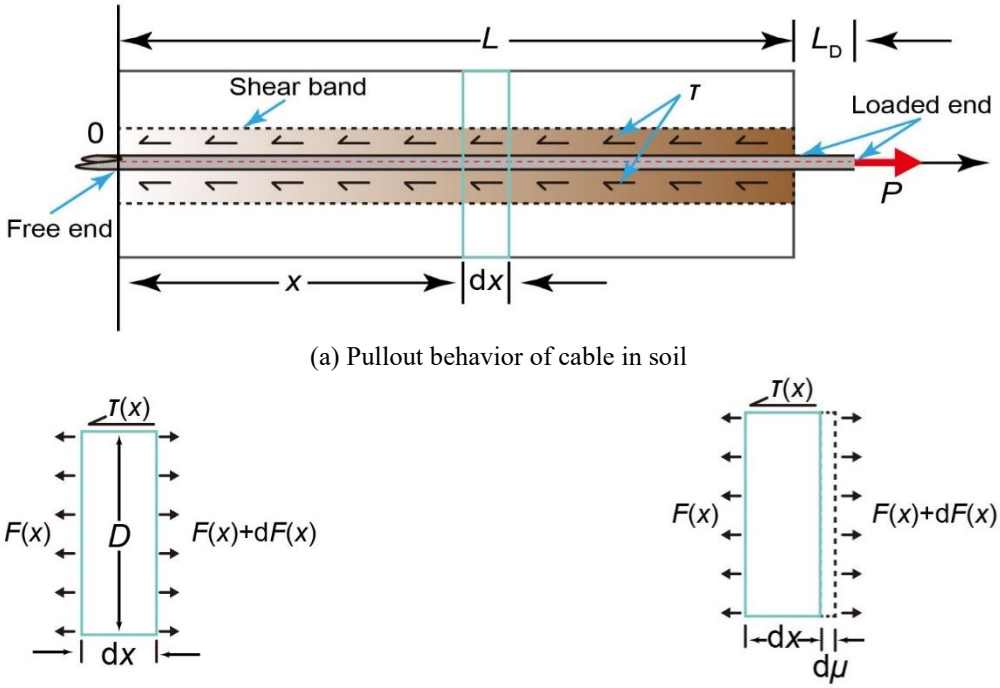

(a) Pullout behavior of cable in soil

(b) Stress state

(c) Deformation mechanism

Fig. 1 Schematic diagram of fiber-optic cable–soil interaction

shear strength comprises primarily the mechanical interlock and friction (Li and Stillborg 1999). Historically, bond–slip models were adopted for the characterization of fiber-reinforced composites and anchor bolts. For instance, Cai *et al.* (2004) used a bi-linear elastoplastic model to simulate the interface failure of frictional bolts and grout for a CFC system, which can provide a reference to soil-embedded cables simplified as extensible cylindrical bolts. More recently, Zhang *et al.* (2016) proposed an elastoplastic model for describing the progressive pullout failure of cables in soil. The analytical predictions agreed with both experimental pullout force–displacement curves and cable axial strain profiles for a 2-mm-diameter cable buried in a 1500×200×200 mm soil tank. While the cable–soil interface shear strength as a common proxy can represent how rigid the cable is coupled to its surroundings (ASTM 2014), axial strain distributions along the cable directly related to the progressive failure process of the interface have not been fully exploited. Additionally, the effects of cable and cable–soil interface characteristics on the cable–soil coupling behavior deserve further study.

This study aimed at evaluating the fiber-optic cable–soil mechanical coupling by using an elastoplastic pullout model. First, the classical elastoplastic pullout model was briefly described, yielding two new quantitative indices for cable–soil coupling assessment. Next, a laboratory pullout test was performed on a soil-embedded cable to validate the pullout model. Then, a parametric analysis was conducted to investigate the effects of cable geometric and mechanical parameters and interface shear parameters on the cable–soil mechanical coupling. Finally, suggestions on improving the cable–soil coupling in practice were given, and modifications to the elastoplastic pullout model were discussed to better simulate cable–soil pullout interactions.

2. Overview of the elastoplastic pullout model

2.1 Cable-soil interface mechanical characteristics and analytical expressions

An elastoplastic model proposed by Zhang *et al.* (2016) for describing the pullout behavior of fiber-optic cables in soil is overviewed. Fig. 1 schematically illustrates a soil-embedded cable subjected to a pullout load. The cable is assumed as an axially loaded component while its radial deformation is neglected. Upon loading, the cable–soil interface shear stress is mobilized to resist the pullout force. The pullout displacement (u) of the cable comprises the cable–soil interface shear displacement (u_S) and the tensile deformation of the dangling cable (u_T). For the sake of simplicity, u_T is neglected and, hence, only u_S is considered.

In this model, the relationship between the interface shear stress and the shear displacement follows an ideal bi-linear elastoplastic model (Fig. 2), which can be expressed by:

$$\tau(x) = \begin{cases} G^* u(x) & \text{for } u < u_C \quad (1a) \\ \tau_{\max} & \text{for } u_C \le u \quad (1b) \end{cases} \tag{1}$$

where G^* is the interface shear coefficient defined by the slope of the ascending branch (Unit: MPa/m); $\tau_{\max}$ is the interface shear strength; and u_c is the critical interface shear displacement, $u_C = \tau_{\max}/G^*$.

The pullout process can therefore be divided into three stages according to different interface stress states; schematic distributions of the interface shear stress, axial force, axial strain, and interface shear deformation are depicted in Fig. 3. The analytical expressions for each

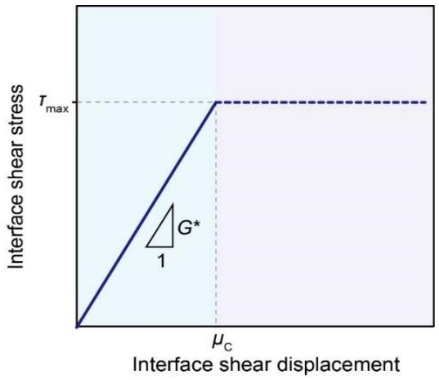

Fig. 2 Constitutive relationship between shear stress and displacement for fiber-optic cable-soil interface

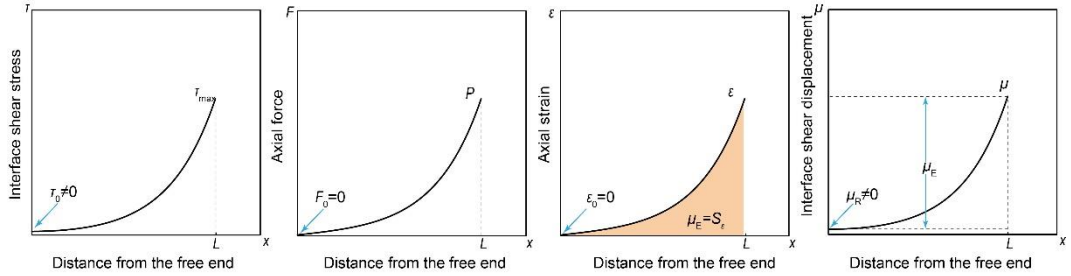

(a) The pure elastic stage

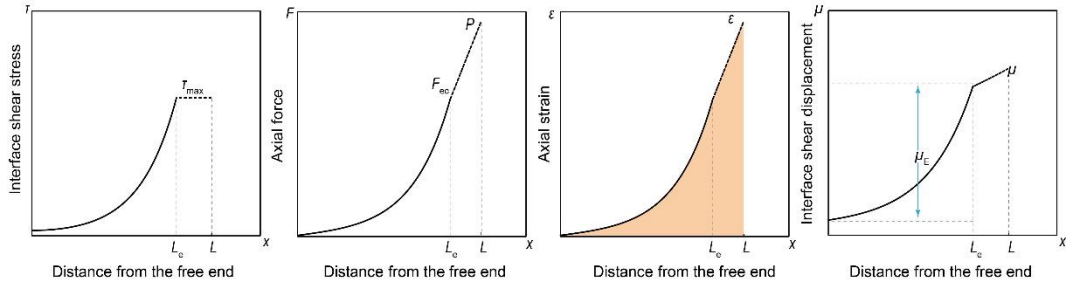

(b) The elastoplastic stage

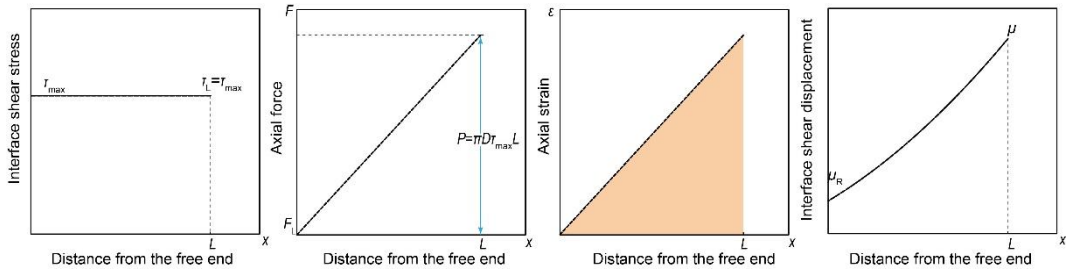

(c) The pure plastic stage

Fig. 3 Fiber-optic cable-soil interface characteristics of all stages

pullout stage are concisely presented in the following. The readers are referred to Zhang *et al.* (2016) for detailed model descriptions and formulations.

2.1.1 Pure elastic stage (Stage I)

In stage I, the boundary conditions are:

$$\begin{cases} F(0) = 0 \\ F(L) = P \end{cases} \tag{2}$$

Then the axial strain and interface shear stress can be expressed as:

$$\varepsilon(x) = \frac{P}{EA}\frac{\sinh \alpha x}{\sinh \alpha L} \tag{3}$$

$$\varepsilon(x) = \frac{P}{EA}\frac{\sinh \alpha x}{\sinh \alpha L} \tag{4}$$

where P is the pullout force; L, E, A, and D are the length, Young's modulus, cross-sectional area, and the diameter of the cable, respectively; and α is the pullout model coefficient, $\alpha = \sqrt{4G^*/(DE)}$.

2.1.2 Elastoplastic stage (Stage II)

In stage II, the interface properties of the elastic segment ($0 \le x \le L_e$) are similar to those in stage I:

$$\varepsilon(x) = \frac{F_{ec}}{EA}\frac{\sinh \alpha x}{\sinh \alpha L_e} \tag{5}$$

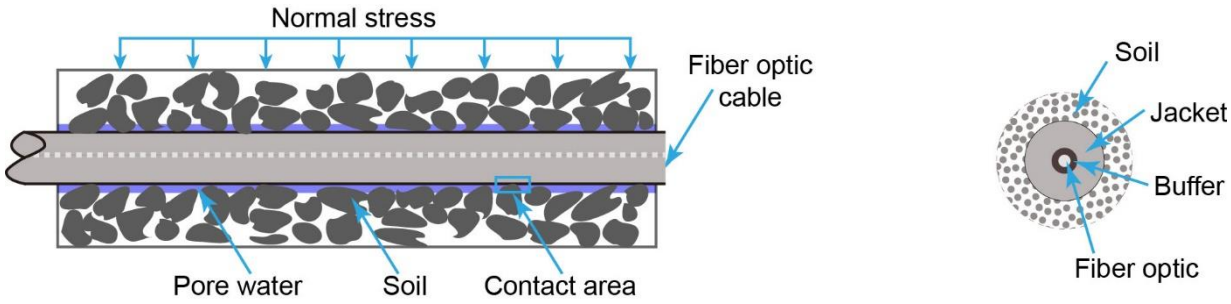

(a) Plane view (b) Cross-sectional view

Fig. 4 Schematic view of fiber-optic cable-soil interface

$$\tau(x) = \frac{\alpha F_{ec}}{\pi D} \frac{\cosh \alpha x}{\sinh \alpha L_e} \quad (6)$$

where L_e is the length of the elastic segment, and F_{ec} is the critical axial force at the transition position from the elastic segment to the plastic segment, $F_{ec} = \pi D \tau_{max} \tanh \alpha L_e / \alpha$.

The interface properties of the plastic segment ($L_e \leq x \leq L$) are as follows:

$$\varepsilon(x) = \frac{F_T}{EA} + \frac{4\tau_{max}}{DE}(x - L_e) \quad (7)$$

$$\tau(x) = \tau_{max} \quad (8)$$

2.1.3 Pure plastic stage (Stage III)

In stage III, the interface shear stress along the entire cable length reaches the shear strength. Hence, we have

$$\varepsilon(x) = \frac{\pi D \tau_{max}}{EA} x \quad (9)$$

$$\tau(x) = \tau_{max} \quad (10)$$

2.2 Quantitative indices for evaluating cable–soil mechanical coupling

For a soil-embedded cable, the mechanical coupling between the cable and the soil depends on the cable–soil interface behavior. The geotechnical community has recognized some crucial factors influencing the mechanical behavior of a soil–inclusion interface, e.g., the normal stress, soil moisture content, soil density, and interface contact area (Fu *et al.* 2000, Hsueh 1992, Landis and McMeeking 1999, Michalowski and Zhao 1996) (Fig. 4). However, it will be a laborious task to assess the cable–soil mechanical coupling by calibrating each parameter. The elastoplastic model described above allows an effective evaluation of the mechanical coupling using shear properties of the cable–soil interface. For instance, the condition of coupling can be evaluated by comparing the interface shear stress with the shear strength (τ_{max})—once the interface shear stress reaches τ_{max}, the interface decouples and the strain present in the soil cannot be fully transferred to the sensing cable (ASTM 2014). In addition to this strength parameter, two other indices are originally proposed in this research to assess quantitatively the cable–soil coupling.

2.2.1 Limit length for strain loss (L_{lim})

Under pullout conditions, the axial strain decreases from the loaded end toward the free end. Experimental evidence suggested that strain propagation will be restrained near the loaded end if the cable–soil coupling is strong (Zhang *et al.* 2018a). In this sense, the limit length for strain loss (L_{lim}) is proposed, which is defined as the distance from the loaded end to where the strain decreases to a strain limit (ε_{lim}, 3% of the strain at the loaded end). Apparently, a shorter limit length means a better coupling condition.

2.2.2 Percentage of rigid body displacement (η)

The rigid body displacement (u_R) is the cable displacement at the free end (Fig. 1(a)). Analysis of this rigid body displacement for cable-soil coupling evaluation purposes is limited in the literature. A third index, rigidity index η, is therefore proposed based on u_R and is defined as follows:

$$\eta = \frac{u_R}{u} \quad (11)$$

where u is the pullout displacement. The greater the percentage of u_R, the larger the relative displacement of full-length cable will be at the cable–soil interface, which indicates a weak mechanical coupling between the cable and the soil.

3. Model validation by pullout test

3.1 Test setup and procedure

Prior to evaluating the cable–soil mechanical coupling using the above indices, a pullout test was conducted to validate the elastoplastic pullout model. Fig. 5 is a photograph showing the experimental setup of the pullout test, which consists of a 1-m-long, 60-mm-diameter cylindrical acrylic tube, a pullout motor, and a measurement system. A fiber-optic cable–soil specimen is prepared in the acrylic tube, which is deployed horizontally. The pullout motor is capable of pulling the cable at a constant speed and the measurement system of recording the pullout force, displacement, and axial strain along the cable at each load step.

A 2-mm-diameter tight-buffered fiber-optic strain-sensing cable was tested, which is made of an acrylate coated optical fiber with a thermoplastic polyurethane

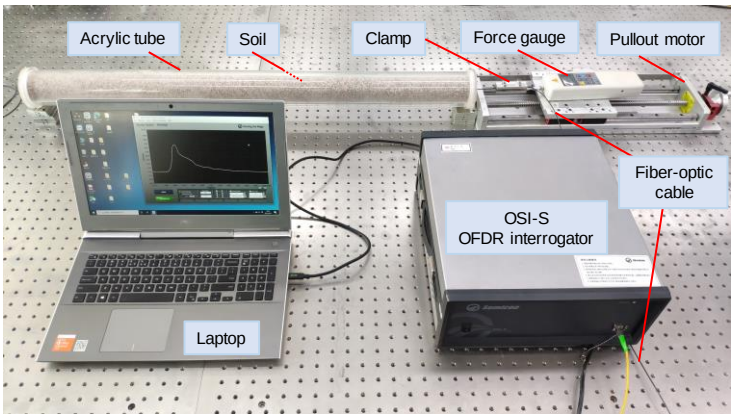

Fig. 5 Pullout apparatus for investigating the fiber-optic cable–soil interaction mechanism

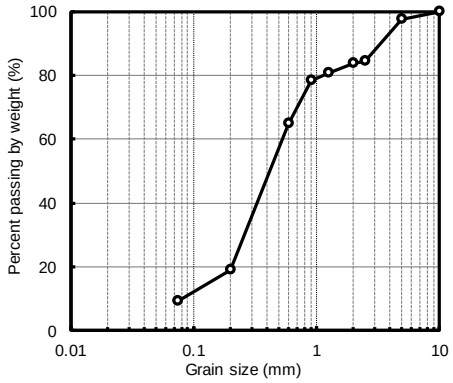

Fig. 6 Grain size distribution of the test soil

Table 1 Parameters of the bi-linear elastoplastic model for simulating the pullout test results

G^* (MPa/m)	τ_{max} (kPa)	α (m^{-1})	D (mm)	L (m)	E (MPa)
2.91	1.49	3.97	2	0.9	370

jacket. The cable has an upper strain limit of approximately 1.5% that the inside silica fiber can accommodate before plastic deformation occurs or breakage. The soil is a mixture of sand, gravel, and clay at a mass ratio of 7.5:2.5:1 with a water content of 14.44%—a backfill that has been used to seal two fiber optics instrumented boreholes for soil strata deformation monitoring (Wu *et al.* 2015, Liu *et al.* 2020). Its grain size distribution is shown in Fig. 6.

The pullout force and displacement were recorded by a force gauge with an accuracy of 0.1 N and a displacement gauge with a resolution of 0.01 mm, respectively. The pullout displacement was applied by the pullout motor with a velocity of 2 mm/min (same as Liu *et al.* (2021b)). The fiber-optic interrogator used was an optical frequency-domain reflectometry (OFDR), model Semicon OSI-S, provided by Wuhan Junno Tech., China, which allowed measuring at a spatial resolution of 10 mm and a strain accuracy of ±1 με.

At first, the OFDR interrogator measured an initial strain as the reference strain. After applying each pullout displacement step of 0.5 mm, the interrogator collected the resulting strain profile, and the pullout force was recorded simultaneously. The test terminated when the pullout force remained constant with increasing displacements, or when the axial strain reached approximately 15,000 με.

3.2 Validation and interpretation

The parameters of the cable and cable–soil interface used to simulate the pullout test results are given in Table 1. Among these six parameters, D, L, and E were the actual cable properties while the interface shear parameters (G^*, τ_{max}, and α) were calibrated by the experimental data using the least-squares fitting.

The measured pullout force–displacement curve was in good agreement with the simulated curve (Fig. 7). A typical strain-hardening behavior was observed during the pullout process. At stage I, the pullout force increased almost linearly with the displacement as the cable was fully bonded to the soil and no interface slip occurred. The feature of stage II was that the increment of pullout force slowed down because of the appearance of transitional failure, i.e., the cable segment close to the loaded end entered the plastic stage while the far end stayed in the elastic stage. Finally, as the pullout displacement reached 3.58 mm, the pullout force remained 8.42 N as the entire cable was in the pure plastic stage.

A comparison between the measured and predicted axial

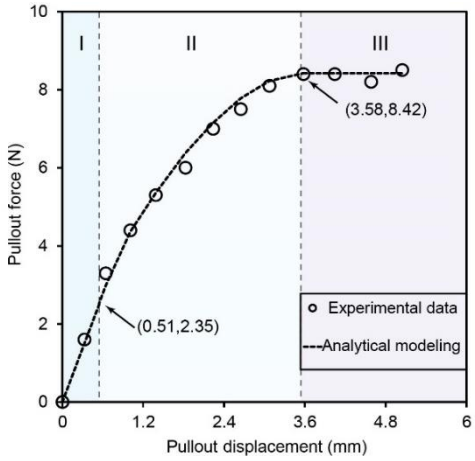

Fig. 7 Comparison between experimental and analytical pullout force-displacement curves

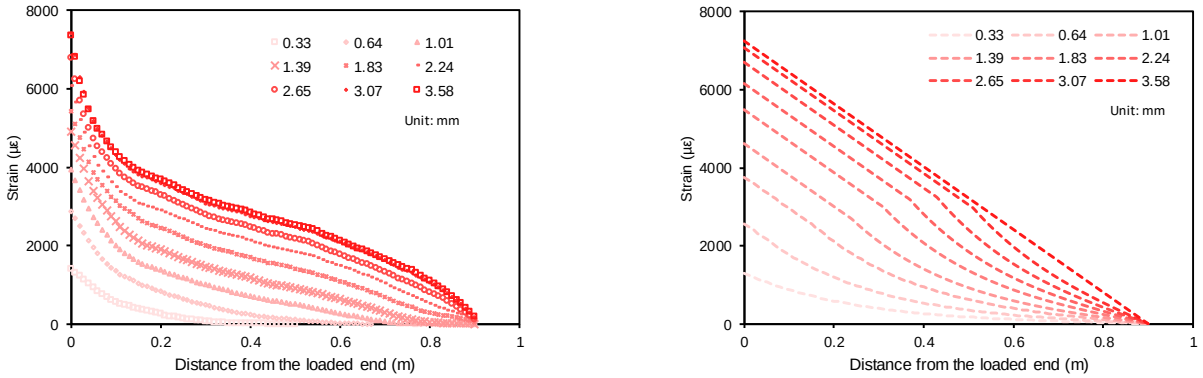

(a) Experimental measurements (b) Analytical predictions

Fig. 8 Comparison between axial strain distributions along fiber-optic cable

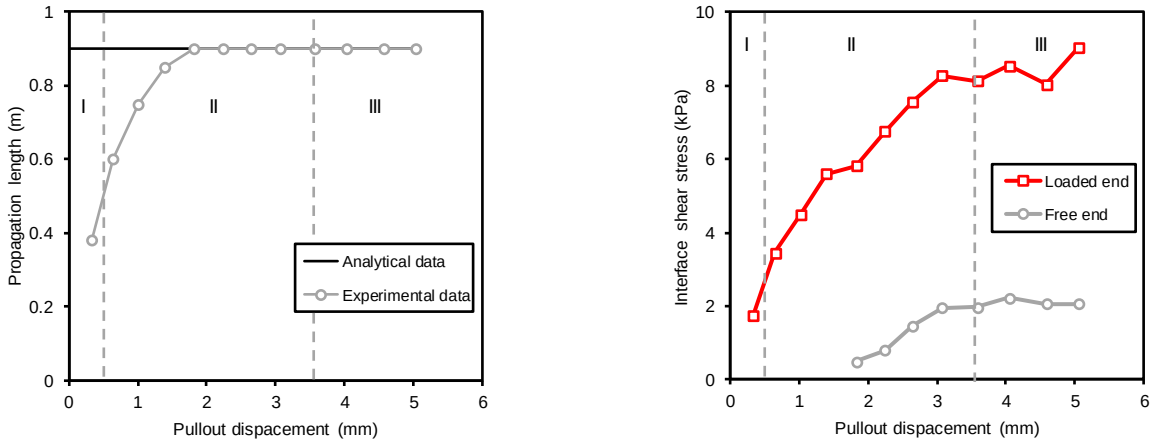

(a) Strain propagation length between analytical modeling and experimental data (b) Interface shear stresses at different segments of cable determined from experimental data

Fig. 9 Interface parameters of analytical modeling and experimental data

strain distributions along the cable is shown in Fig. 8. Two features were evident for both strain profiles: (i) the axial strain propagated and decreased from the loaded end to the free end, and (ii) the axial strain increased with increasing pullout displacements. However, discrepancies were noted in terms of the strain propagation distance. Specifically, the strain propagated to the cable end at a pullout displacement of 1.83 mm in the test while the analytical strain propagation distance appeared to be constant (0.9 m; Fig. 9(a)). A possible explanation for this difference is that the pullout is a dynamic equilibrium process—as the soil gathers at the loaded end during pullout, the local cable–soil interaction will be enhanced and the interface parameters will be improved (Al-Khazaali and Vanapalli 2019). This was evidenced from the interface shear stresses estimated at two different segments of the cable—the interface shear

Table 2 Interface geometric and mechanical parameters used in the parametric analysis

No.	G^* (MPa/m)	τ_{max} (kPa)	D (mm)	L (m)	E (MPa)	Fig.
Scenario 1	5, 10, 15	2.7	2	1	370	10(a)
Scenario 2	1, 5, 10, 50, 100	—	2	1	370	10(b)–(e)
Scenario 3	5	—	1, 2, 4	1	370	11
Scenario 4	5	—	2	0.5, 1, 5, 10	370	12
Scenario 5	5	—	2	1	370, 740, 1110	13

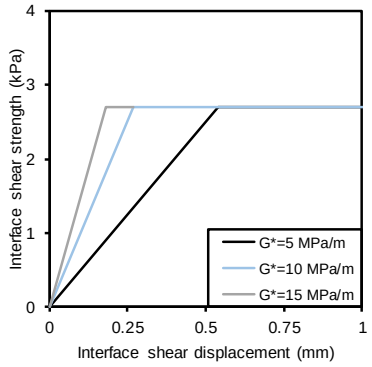

(a) Interface shear constitutive relationship

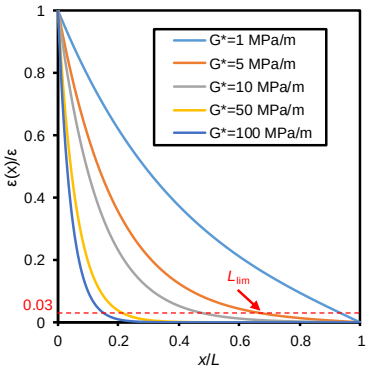

(b) Normalized strain distribution

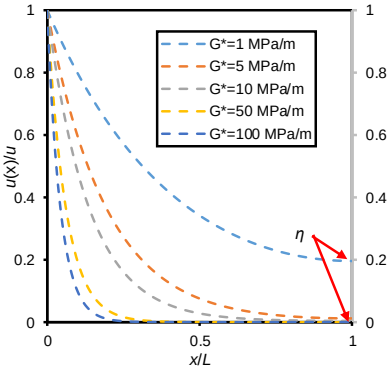

(c) Normalized interface shear displacement distribution

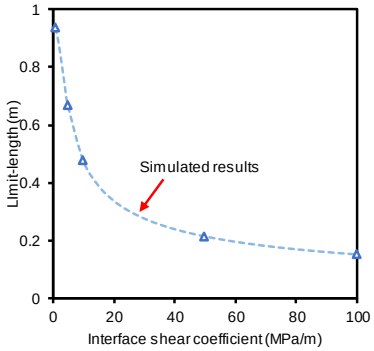

(d) Relationship between limit length and interface shear coefficient

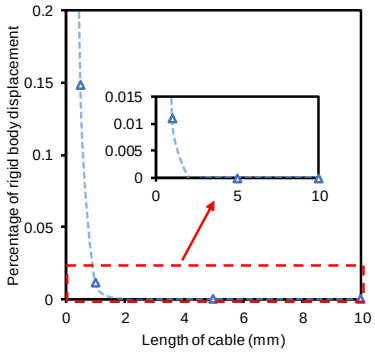

(e) Relationship between percentage of rigid body displacement and interface shear coefficient

Fig. 10 Influence of interface shear coefficient on fiber-optic cable–soil mechanical coupling

stresses at the loaded end and the free end rose to different constant values with increasing pullout displacements, rather than the same value that would be predicted using the elastoplastic pullout model (Fig. 9(b)). Note that although this effect has not been considered in the analytical model, the assumption of uniformly distributed interface properties is sufficient to evaluate the cable–soil mechanical coupling from a practical point of view.

4. Parametric study

Parametric analysis was conducted to investigate the effects of cable geometric and mechanical parameters (D, L,

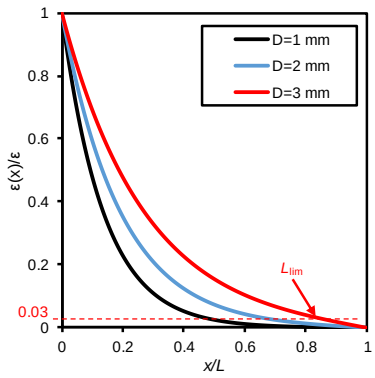

(a) Normalized strain distribution

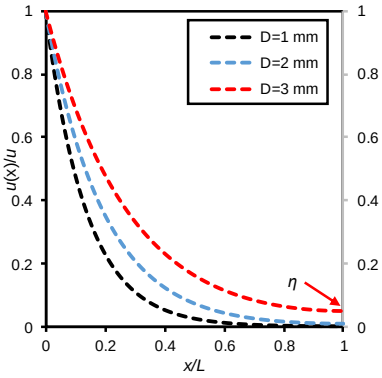

(b) Normalized interface shear displacement distribution

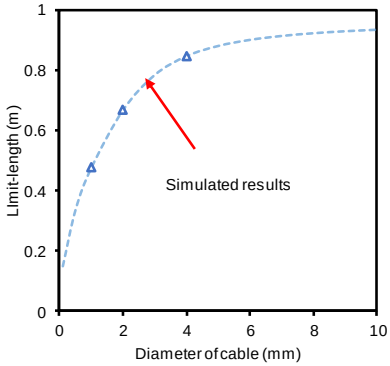

(c) Relationship between limit length and cable diameter

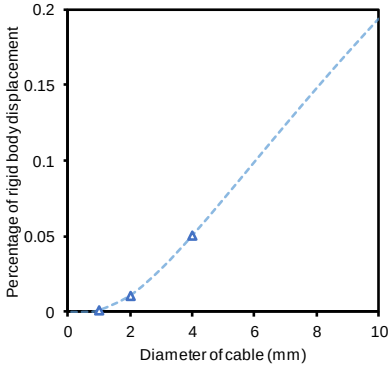

(d) Relationship between percentage of rigid body displacement and cable diameter

Fig. 11 Influence of fiber-optic cable diameter on cable–soil mechanical coupling

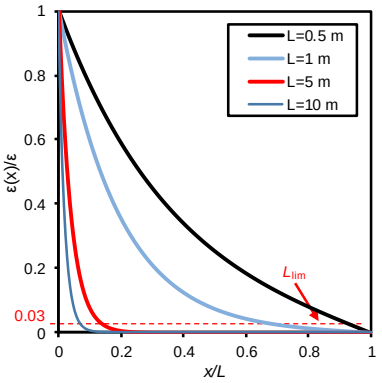

(a) Normalized strain distribution

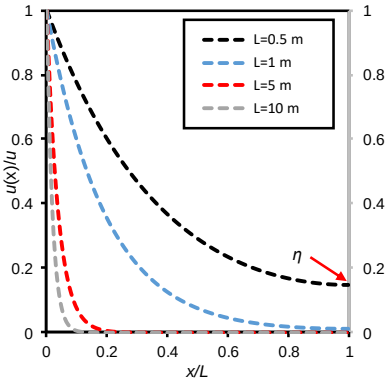

(b) Normalized interface shear displacement distribution

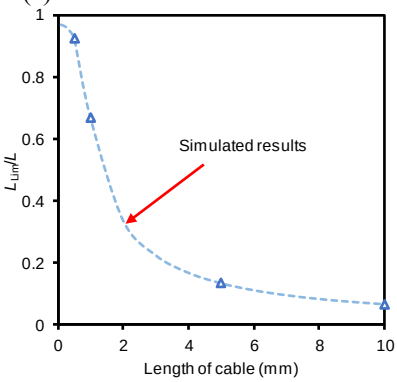

(c) Relationship between limit length and cable embedment length

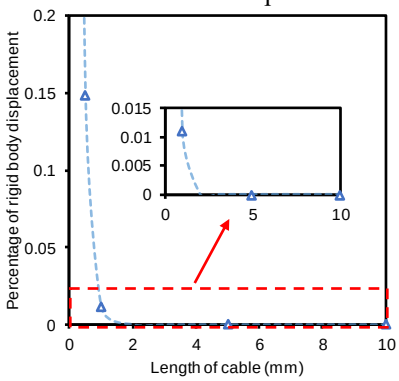

(d) Relationship between percentage of rigid body displacement and cable embedment length

Fig. 12 Influence of fiber-optic cable embedment length on cable-soil mechanical coupling

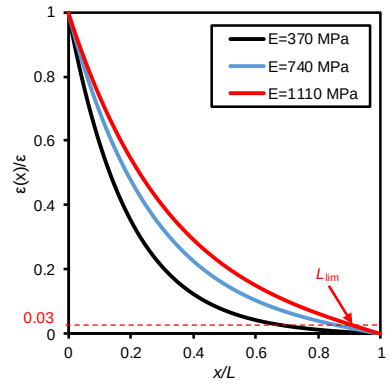

(a) Normalized strain distribution

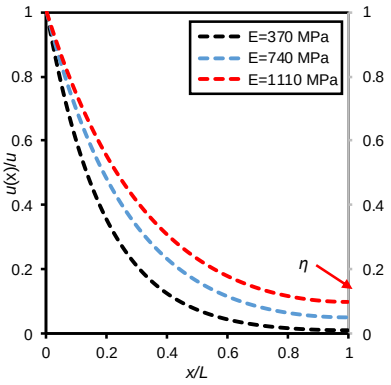

(b) Normalized interface shear displacement distribution

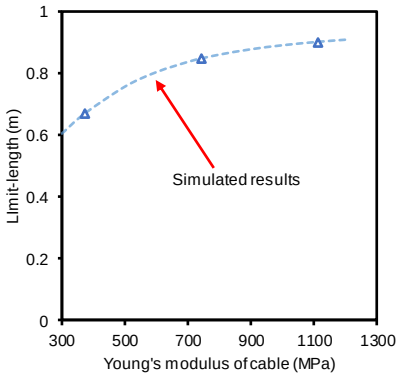

(c) Relationship between limit length and cable Young's modulus

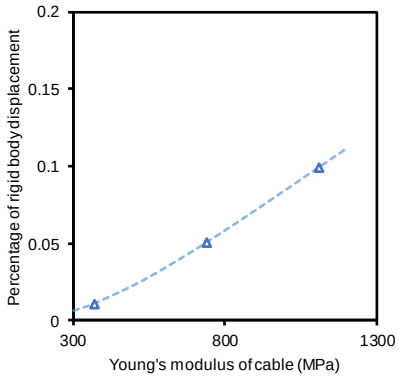

(d) Relationship between percentage of rigid body displacement and cable Young's modulus

Fig. 13 Influence of fiber-optic cable Young's modulus on cable-soil mechanical coupling

and E) and interface shear parameters (G^*) on the cable–soil mechanical coupling. The values of these parameters are within typical ranges according to the literatures (Iten *at al.* 2009 and 2011, Wu *et al.* 2014, Liu *et al.* 2021b), which are summarized in Table 2.

The influence of interface shear coefficient (G^*) on the pullout behavior is illustrated in Fig. 10. Fig. 10(a) shows that the total pullout displacement generated in stage I decreased with the increase of G^*. Obviously, the shear strength criterion is unsuitable for assessing the mechanical coupling behavior in this case while the proposed two indices can be used to evaluate the interaction. In order to better elucidate the influence of G^*, Figs. 10(b)–(c) depict the axial strain and interface shear displacement distributions at different values of G^*. With a large G^* value, the axial strain and shear displacement profiles declined sharply near the loaded end. For example, the strain decreased by 38%, 97%, and 99% when propagating a distance of $0.2L$ with G^* values of 1 MPa/m, 50 MPa/m, and 100 MPa/m, respectively. It is obvious in Figs. 10(d)–(e) that both the limit length (L_{lim}) and rigid body displacement percentage (η) increased with increasing G^*, with a decreasing rate. Note that the dashed line represents the simulated results with finer G^* increment than that listed in Table 2. Therefore, a higher G^* can contribute to a stronger cable–soil coupling in terms of the L_{lim} and η criterion.

The effects of diameter and embedded length of cable on the pullout behavior are shown in Figs. 11 and 12. It is readily observed that a large cable diameter corresponded to a large limit length and rigid body displacement percentage. By contrast, the longer the cable embedded in soil, the smaller limit length and rigid body displacement percentage will be. This finding indicates that a small diameter and a long embedment length are preferable in terms of ensuring a strong mechanical coupling of the cable–soil interface.

Besides the geometric characteristics, the mechanical property of cable (i.e., the Young's modulus, E) is another key influencing factor. Figs. 13(a) and 13(b) depict the influence of E on the pullout behavior of soil-embedded cable. A low E may help reduce the L_{lim} and η values and, hence, improve the mechanical coupling between cable and soil (Figs. 13(c) and 13(d)).

In summary, the influences of key parameters of the elastoplastic pullout model on the cable–soil mechanical coupling were investigated. The results indicate that a fiber-optic cable with small diameter, large embedment length, and low Young's modulus can contribute to a strong interaction with its surrounding soil. In addition, increasing the interface shear coefficient may help improve the performance of strain transfer.

5. Discussion

5.1 Improving the cable-soil coupling in practice

The findings from the parametric study may guide the design of fiber-optic cables for soil deformation monitoring.

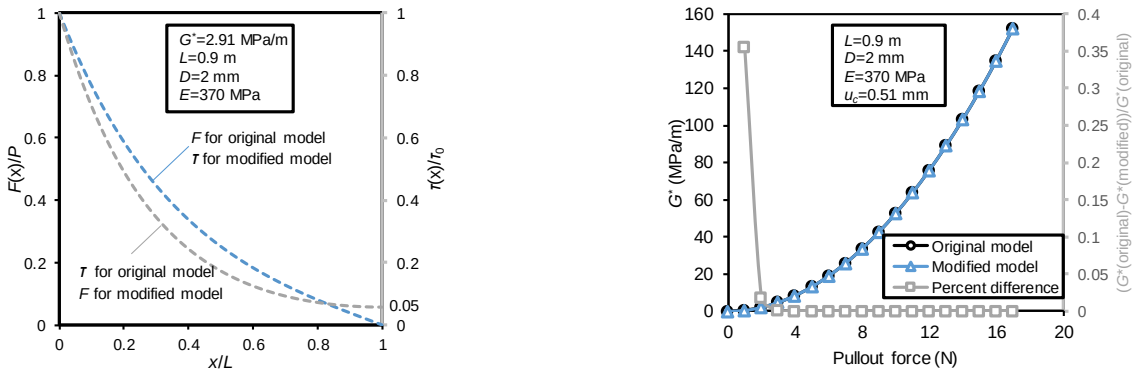

(a) Interface stress transfer (b) Interface shear coefficient

Fig. 14 Comparisons between original and modified bi-linear elastoplastic models

In a certain scenario, the embedment length of a cable is fixed for a monitored target. Therefore, it is mainly through changing D or E of the cable to improve the performance of a DSS system. Theoretically, a thin and flexible cable can contribute to better cable–soil coupling (Figs. 11 and 13). In practice, however, the cable should be of sufficient stiffness to survive the installation process and the harsh subsurface environment. In our pullout test, the cable with D = 2 mm and E = 0.37 GPa was used (for Iten (2011)'s pullout test, D = 2.8 mm and E = 0.47 GPa), which seems sufficient for use in the laboratory. Cables with smaller diameter (D = 0.9 mm, E = 3.1 GPa) are fragile and should therefore be adhered to, for example, PVC piles (see Moffat *et al.* (2015)). Recently, a cable with a protective steel conduit (D = 5 mm, E = 0.076 GPa) was successfully deployed in a 100-m-deep borehole for subsidence monitoring in a coastal setting for nearly 20 months (Liu *et al.* 2020). Therefore, the geometric and mechanical properties of the cable should be determined based on specific applications. In summary, a fiber-optic cable with a diameter of 2–3 mm and a relatively low Young's modulus of 0.3–0.4 GPa is capable of ensuring a good strain measurement in laboratory tests, while the diameter should be increased with protective reinforcements for monitoring soil deformation in the field.

Secondly, the parameter G^* is closely related to the cable–soil interface characteristics according to previous cable or soil inclusion experiments, which can be improved by reducing the soil moisture content (Zhang *et al.* 2016) or by increasing the soil relative density (Tang *et al.* 2010), confining pressure (Al-Khazaali and Vanapalli 2019), and surface roughness (Tehrani *et al.* 2016, Sharma *et al.* 2017).

5.2 Toward better modeling of cable–soil pullout interaction

In modeling the mechanical behavior of the cable–soil interface, one assumption is that the axial force at the cable toe is zero (Eq. (2)), which is commonly adopted in other simplified elastoplastic interface models (Naaman *et al.* 1991, Cai *et al.* 2004). However, this assumption will inevitably lead to a rigid body displacement (u_R). For instance, a 5.5% of pullout displacement was regarded as u_R during modeling of the test result, irrespective of the pullout displacement applied, which does not conform to the real situation. Here, an attempt is made to modify the boundary condition. If the interface shear displacement at the free end is assumed to be zero, then Eq. (2) can be expressed by:

$$\begin{cases} F(0) = P \\ \dfrac{dF(L)}{dx} = 0 \end{cases} \tag{12}$$

Accordingly, the following closed-form solutions can be obtained:

$$\varepsilon(x) = \frac{P}{EA}\frac{\cosh \alpha x}{\cosh \alpha L} \tag{13}$$

$$\tau(x) = \frac{\alpha P}{\pi D}\frac{\sinh \alpha x}{\cosh \alpha L} \tag{14}$$

Fig. 14(a) illustrates the distributions of normalized strain and shear stress along the cable using both the original and modified models. The results show that the transfer trend of ε (or τ) in the original model is the same as that of τ (respectively, ε) in the modified model. To compare the two models, the G^* values under the same pullout force at stage I are calculated (Fig. 14(b)). It can be observed that the effect of boundary condition on the calibration of G^* values is negligible once the experimental pullout force exceeds 2 N.

Therefore, a short embedment length, high Young's modulus, and large diameter of cable and a loose soil (low G^*) are more likely to cause the rigid body displacement, which can be better modeled by using the original model. By contrast, when emphasizing the toe displacement and displacement profile along the cable, the modified model may be preferred. Note that the effect of boundary conditions on the calibration of interface parameters can be determined by the pullout force values (e.g., Fig. 14(b)).

The difference in interaction behavior between the experimental observation and analytical simulation has been attributed to the nonuniform distribution of the interface shear parameters (Figs. 8 and 9), owing to the shear dilation effect. Further modification of the constitutive relationship of the cable–soil interface should be made for a better evaluation of the cable–soil mechanical coupling.

6. Conclusions

The complicated interaction between a fiber-optic

strain-sensing cable and surrounding soil is a key factor affecting the quality of soil strains measured with the DSS technology. In this paper, the elastoplastic pullout model was employed to evaluate the fiber-optic cable–soil mechanical coupling. The main findings of this study are the following:

• General good agreement between experimental data (pullout force–displacement curve and cable axial strain distributions) and analytical predictions was found for a 2-mm-diameter fiber-optic cable pulled out from a sand–gravel–clay mixture, validating the elastoplastic model for describing the pullout behavior of soil-embedded cables. The observed discrepancy between the two results was attributed to the nonuniform distribution of interface shear properties.

• Two new indices (L_{lim} and η) were proposed for cable–soil coupling assessment according to the elastoplastic model. L_{lim} is the limit length for strain loss while η is the percentage of rigid body displacement, leveraging cable axial strain profiles and cable–soil relative displacement measurements, respectively. Both the two indices can quantify the cable–soil mechanical coupling, in addition to the commonly adopted interface shear strength proxy.

• Results of the parametric study showed that a fiber-optic cable with small diameter, large embedment length, low Young's modulus, and large interface shear coefficient can contribute to a strong interaction with surrounding soil. In practice, a fiber-optic cable with a diameter of 2–3 mm and a relatively low Young's modulus of 0.3–0.4 GPa can ensure a good strain measurement in laboratory tests, while the diameter should be increased with protective reinforcements for use in the field.

• Modification to the boundary condition of the original model yielded new expressions for cable axial strain and cable–soil interface shear stress, which apply to the situation where the rigid body displacement is of interest. Choice of the original or modified model depends on the pullout force value.

Acknowledgments

This work was supported by the National Natural Science Foundation of China (NSFC) grants 42030701 and 41427801 to B.S. C.-C.Z. acknowledges support by the Natural Science Foundation of Jiangsu Province grant BK20200217 and the Yuxiu Young Scholars Program of Nanjing University. K.G. acknowledges support by NSFC grant 41977217. S.-P.L. acknowledges support by the Postgraduate Research & Practice Innovation Program of Jiangsu Province grant KYCX19_0048 and the China Scholarship Council. S.-P.L. would like to thank Professor Hai-Sui Yu for his supervision and assistance at the University of Leeds.

References

Al-Khazaali, M. and Vanapalli, S.K. (2019), "Axial force–displacement behaviour of a buried pipeline in saturated and unsaturated sand", *Géotechnique*, **69**(11), 986-1003. https://doi.org/10.1680/jgeot.17.P.116.

Ashtiani, M., Ghalandarzadeh, A., Mahdavi, M. and Hedayati, M. (2018), "Centrifuge modeling of geotechnical mitigation measures for shallow foundations subjected to reverse faulting", *Can. Geotech. J.*, **55**(8), 1130-1143. https://doi.org/10.1139/cgj-2017-0093.

ASTM F3079-14. (2014), Standard practice for use of distributed optical fiber sensing systems for monitoring the impact of ground movements during tunnel and utility construction on existing underground utilities, ASTM International, West Conshohocken, PA, U.S.A.

Billon, A., Hénault, J.M., Quiertant, M., Taillade, F., Khadour, A., Martin, R.P. and Benzarti, K. (2015), "Qualification of a distributed optical fiber sensor bonded to the surface of a concrete structure: A methodology to obtain quantitative strain measurements", *Smart Mater. Struct.*, **24**(11), 115001.

Cai, Y., Esaki, T. and Jiang, Y. (2004), "A rock bolt and rock mass interaction model", *Int. J. Rock Mech. Min. Sci.*, **41**(7), 1055-1067. https://doi.org/10.1016/j.ijrmms.2004.04.005.

Friedli, B., Pizzetti, L., Hauswirth, D. and Puzrin, A.M. (2019), "Ground-buried fiber-optic sensors for object identification", *J. Geotech. Geoenviron. Eng.*, **145**(2), 04018109. https://doi.org/10.1061/(asce)gt.1943-5606.0002001.

Fu, S.Y., Yue, C.Y., Hu, X. and Mai, Y.W. (2000), "Analyses of the micromechanics of stress transfer in single- and multi-fiber pull-out tests", *Compos. Sci. Technol.*, **60**(4), 569-579. https://doi.org/10.1016/s0266-3538(99)00157-8.

Habel, W.R. and Krebber, K. (2011), "Fiber-optic sensor applications in civil and geotechnical engineering", *Photonic Sensors*, **1**(3), 268-280. https://doi.org/10.1007/s13320-011-0011-x.

Hauswirth, D., Puzrin, A.M., Carrera, A., Standing, J.R. and Wan, M.S.P. (2014), "Use of fibre-optic sensors for simple assessment of ground surface displacements during tunnelling", *Géotechnique*, **64**(10), 837-842. https://doi.org/10.1680/geot.14.T.009.

Hsueh, C.H. (1992), "Interfacial debonding and fiber pull-out stresses of fiber-reinforced composites VII:improved analyses for bonded interfaces", *Mater. Sci. Eng. A*, **154**(2), 125-132. https://doi.org/10.1016/0921-5093(92)90337-z.

Iten, M. (2011), "Novel application of distributed fiber-optic sensing in geotechnical engineering", Ph.D. Dissertation. ETH Zurich, Zurich, Switzerland.

Iten, M., Puzrin, A.M., Hauswirth, D., Foaleng-Mafang, S., Beugnot, J.C. and Thévenaz, L. (2009), "Study of a progressive failure in soil using BEDS", *Proceedings of the 20th International Conference on Optical Fibre Sensors*, Edinburgh, U.K., October.

Landis, C.M. and Mcmeeking, R.M. (1999), "A shear-lag model for a broken fiber embedded in a composite with a ductile matrix", *Compos. Sci. Technol.*, **59**(3), 447-457. https://doi.org/10.1016/s0266-3538(98)00091-8.

Lanticq, V., Bourgeois, E., Magnien, P., Dieleman, L., Vinceslas, G., Sang, A. and Delepine-Lesoille, S. (2009), "Soil-embedded optical fiber sensing cable interrogated by Brillouin optical time-domain reflectometry (B-OTDR) and optical frequency-domain reflectometry (OFDR) for embedded cavity detection and sinkhole warning system", *Measurement Sci. Technol.*, **20**(3), 034018. https://doi.org/10.1088/0957-0233/20/3/034018.

Li, B., Zhang, D., Chen, X., Wang, J. and Shi, B. (2017), "Testing method on performance of deformation coupling between distributed sensing fiber and soil", *Geol. J. China Univ.*, **23**(4), 633-639.

Li, C. and Stillborg, B. (1999), "Analytical models for rock bolts", *Int. J. Rock Mech. Min. Sci.*, **36**(8), 1013-1029. https://doi.org/10.1016/s1365-1609(99)00064-7.

Liu, S. P., Shi, B., Gu, K., Zhang, C. C., Yang, J. L., Zhang, S. and

Yang, P. (2020), "Land subsidence monitoring in sinking coastal areas using distributed fiber optic sensing: A case study", *Nat. Hazards*, **103**(3), 3043-3061. https://doi.org/10.1007/s11069-020-04118-1.

Liu, S.P., Shi, B., Gu, K., Zhang, C.C., He, J.H., Wu, J.H., and Wei, G. Q. (2021a), "Fiber-optic wireless sensor network using ultra-weak fiber Bragg gratings for vertical subsurface deformation monitoring", *Nat. Hazards*, 1-17. https://doi.org/10.1007/s11069-021-04932-1.

Liu, S.P., Gu, K., Zhang, C.C. and Shi, B. (2021b), "Experimental research on strain transfer behavior of fiber-optic cable embedded in soil using distributed strain sensing", *Int. J. Geomech.*, **21**(10), 04021190. https://doi.org/10.1061/(ASCE)GM.1943-5622.0002155.

Michalowski, R.L. and Zhao, A. (1996), "Failure of fiber-reinforced granular soils", *J. Geotech. Eng.*, **122**(3), 226-234. https://doi.org/10.1061/(ASCE)0733-9410(1996)122:3(226).

Moffat, R.A., Beltran, J.F. and Herrera, R. (2015), "Applications of BOTDR fiber optics to the monitoring of underground structures", *Geomech. Eng.*, **9**(3), 397-414. http://doi.org/10.12989/gae.2015.9.3.397.

Mohamad, H., Bennett, P.J., Soga, K., Mair, R.J. and Bowers, K. (2010), "Behaviour of an old masonry tunnel due to tunnelling-induced ground settlement", *Géotechnique*, **60**(12), 927-938. https://doi.org/10.1680/geot.8.P.074.

Naaman, A.E., Namur, G.G., Alwan, J.M. and Najm, H.S. (1991), "Fiber pullout and bond slip. I: Analytical study", *J. Struct. Eng.*, **117**(9), 2769-2790. https://doi.org/10.1061/(asce)0733-9445(1991)117:9(2769).

Ni, P., Moore, I.D. and Take, W.A. (2018), "Distributed fibre optic sensing of strains on buried full-scale PVC pipelines crossing a normal fault", *Géotechnique*, **68**(1), 1-17. https://doi.org/10.1680/jgeot.16.P.161.

Pelecanos, L., Soga, K., Elshafie, M.Z.E.B., de Battista, N., Kechavarzi, C., Gue, C.Y., Ouyang, Y. and Seo, H.J. (2018), "Distributed fiber optic sensing of axially loaded bored piles", *J. Geotech. Geoenviron. Eng.*, **144**(3), 04017122. https://doi.org/10.1061/(ASCE)GT.1943-5606.0001843.

Puzrin, A. M., Iten, M. and Fischli, F. (2020), "Monitoring of ground displacements using borehole-embedded distributed fibre optic sensors", *Quart. J. Eng. Geol. Hydrogeol.*, **53**(1), 31-38. https://doi.org/10.1144/qjegh2018-166.

Schenato, L. (2017), "A review of distributed fibre optic sensors for geo-hydrological applications", *Appl. Sci.*, **7**(9), 896. https://doi.org/10.3390/app7090896.

Sharma, M., Samanta, M. and Sarkar, S. (2017), "Laboratory study on pullout capacity of helical soil nail in cohesionless soil", *Can. Geotech. J.*, **54**(10), 1482-1495. https://doi.org/10.1139/cgj-2016-0243.

Soga, K., Ewais, A., Fern, J. and Park, J. (2019), *Advances in Geotechnical Sensors and Monitoring*, in *Geotechnical Fundamentals for Addressing New World Challenges*, 29-65.

Szwedzicki, T. (2001), "Geotechnical precursors to large-scale ground collapse in mines", *Int. J. Rock Mech. Min. Sci.*, **38**(7), 957-965. https://doi.org/10.1016/s1365-1609(01)00062-4.

Tang, C.S., Shi, B. and Zhao, L.Z. (2010), "Interfacial shear strength of fiber reinforced soil", *Geotext. Geomembranes*, **28**(1), 54-62. https://doi.org/10.1016/j.geotexmem.2009.10.001.

Tehrani, F.S., Han, F., Salgado, R., Prezzi, M., Tovar, R.D. and Castro, A.G. (2016), "Effect of surface roughness on the shaft resistance of non-displacement piles embedded in sand", *Géotechnique*, **66**(5), 386-400. https://doi.org/10.1680/jgeot.15.P.007.

Wang, J.C., Zhu, H.H., Shi, B. and Garg, A. (2020), "Strain-based stability analysis of locally loaded slopes under variable conditions", *Geomech. Eng.*, **23**(3), 289-300. https://doi.org/10.12989/gae.2020.23.3.289.

Winters, K.E., Quinn, M.C. and Taylor, O.D.S. (2020), "Assessing the frictional resistance between fiber-optic sensor cable and different soil types", *Proceedings of the Geo-Congress 2020: Modeling, Geomaterials, and Site Characterization*, Minneapolis, Minnesota, U.S.A., February.

Wu, J., Jiang, H., Su, J., Shi, B., Jiang, Y. and Gu, K. (2015), "Application of distributed fiber optic sensing technique in land subsidence monitoring", *J. Civ. Struct. Health Monit.*, **5**(5), 587-597. https://doi.org/10.1007/s13349-015-0133-8.

Yang, X.L. and Wang, H.Y. (2018), "Catastrophe analysis of active-passive mechanisms for shallow tunnels with settlement", *Geomech. Eng.*, **15**(1), 621-630. https://doi.org/10.12989/GAE.2018.15.1.621.

Zhang, C.C., Shi, B., Gu, K., Liu, S.P., Wu, J.H., Zhang, S., Zhang, L., Jiang, H.T. and Wei, G.Q. (2018a), "Vertically distributed sensing of deformation using fiber optic sensing", *Geophys. Res. Lett.*, **45**(21), 11732-11741. https://doi.org/10.1029/2018gl080428.

Zhang, C.C., Shi, B., Zhu, H.H., Wang, B.J. and Wei, G.Q. (2020), "Toward distributed fiber-optic sensing of subsurface deformation: A theoretical quantification of ground-borehole-cable interaction", *J. Geophys. Res. Solid Earth*, **125**(3), e2019JB018878. https://doi.org/10.1029/2019JB018878.

Zhang, C. C., Zhu, H. H., Liu, S. P., Shi, B. and Zhang, D. (2018b), "A kinematic method for calculating shear displacements of landslides using distributed fiber optic strain measurements", *Eng. Geol.*, **234**, 83-96. https://doi.org/10.1016/j.enggeo.2018.01.002.

Zhang, C.C., Zhu, H.H. and Shi, B. (2016), "Role of the interface between distributed fibre optic strain sensor and soil in ground deformation measurement", *Sci. Reports*, **6**, 36469. https://doi.org/10.1038/srep36469.

GC